Centrifuge and Numerical Modeling of the Seismic Response of Buried Water Supply Reservoirs

Karim AlKhatib, S.M.ASCE[1]; Youssef M. A. Hashash, Ph.D., P.E., NAE, F.ASCE[2];
Katerina Ziotopoulou, Ph.D., P.E., M.ASCE[3]; and James Heins, A.M.ASCE[4]

Abstract: Buried water reservoirs are increasingly being built to replace open aboveground municipal water supply reservoirs in urban areas to enhance water quality and utilize their surface footprint for other purposes such as public parks or placement of solar arrays. Many of these lifeline structures are in seismically active regions and, as such, need to be designed to remain operational after severe earthquake shaking. However, evaluating their seismic response is challenging and involves accounting for the interaction of the structure with the stored fluid and the retained soil; in other words, accounting for fluid–structure–soil interaction (FSSI). This paper presents a combined experimental–numerical study on the seismic behavior of buried water reservoirs while considering FSSI. Two series of centrifuge model tests were performed at different reservoir orientations to investigate one-dimensional (1D) and two-dimensional (2D) motion effects under full, half-full, and empty reservoir conditions. Corresponding numerical models were developed whereby the structure and the soil were represented by continuum Lagrangian finite elements, while the fluid was modeled via Arbitrary Lagrangian Eulerian formulation. Soil–structure and fluid–structure interface parameters were calibrated using the experimental measurements. The simulations successfully captured the measured reservoir responses in terms of accelerations, bending moment increments, and water pressures. The study found that the common assumption of plane strain is not applicable for reservoirs because their behavior was found to be truly three-dimensional (3D) whereby stresses accumulated at the corners. Furthermore, the full reservoir resulted in the highest seismic demands in the reservoir walls and roof while the empty reservoir yielded the highest base slippage. The study demonstrates that the complex reservoir seismic response is best captured by carrying out a 3D FSSI numerical simulation. **DOI: 10.1061/JGGEFK.GTENG-11758.**

Introduction

Many US cities, including those located on the West Coast that are subject to high levels of seismicity (e.g., Seattle, San Francisco, and Los Angeles), are now relying heavily on buried water reservoirs to store and supply water. Reservoirs are often located at high ground elevations and shallow depths in order to take advantage of gravity to deliver water (Fig. 1). This implies that a seismic failure might not only cut off the water supply but also release impounded water and debris that can potentially cause massive destruction and flooding to the nearby residential areas, with significant potential for loss of life. Furthermore, such lifeline infrastructures must remain operational following an earthquake to support a city's rapid recovery by maintaining active water supply and delivering water for firefighting.

Buried reservoirs are a relatively new class of structures, and this creates three important implications: (1) they have not yet experienced large earthquakes, (2) code-based or simplified methods are not directly applicable or technically justified for such structures (Cheng et al. 2017), and (3) any advanced three-dimensional (3D) nonlinear fluid–structure–soil interaction (FSSI) analysis has no experimental or case history validation basis. These facts indicate that generalizing the current seismic design practice of underground structures to buried water reservoirs may not be straightforward. A similarly buried reservoir had experienced a catastrophic failure during the M_w 6.6 San Fernando Valley Earthquake in 1971 (Jennings 1971). In that case history, the walls, roof slab, and floor slab were severely damaged especially along the construction joints. The columns were also damaged both at their top and bottom. The peak ground acceleration (PGA) at the site was estimated in the range of 0.3−0.5 g and the preliminary measurements showed differential movement as a consequence of consolidation and sliding produced by the ground shaking. Overall, the current practice of designing buried reservoirs has limitations. Such limitations need to be addressed in a systematic way for the profession to reliably use numerical modeling tools and fully realize the benefits of performance-based engineering in the design and construction of such complex but important lifeline structures.

Experimental and numerical modeling has proven to be a useful tool to examine complex problems involving soil–structure interaction (SSI). Hushmand et al. (2016) conducted centrifuge model tests to evaluate the seismic SSI response of two-dimensional (2D) simplified representations of buried reservoirs. They concluded that none of the available simplified procedures could capture the magnitude and distribution of seismic earth pressures experienced by

---

[1] Graduate Student, Dept. of Civil and Environmental Engineering, Univ. of Illinois Urbana-Champaign, 205 N. Mathews Ave., Urbana, IL 61801. Email: kka2@illinois.edu

[2] Professor, Dept. of Civil and Environmental Engineering, Univ. of Illinois Urbana-Champaign, 205 N. Mathews Ave., Urbana, IL 61801. ORCID: https://orcid.org/0000-0002-0756-9027. Email: hashash@illinois.edu

[3] Associate Professor, Dept. of Civil and Environmental Engineering, Univ. of California Davis, One Shields Ave., Davis, CA 95616 (corresponding author). ORCID: https://orcid.org/0000-0001-5494-497X. Email: kziotopoulou@ucdavis.edu

[4] Engineer, GeoPentech Inc., 101 Academy Dr., Irvine, CA 92617. Email: james_heins@geopentech.com

Note. This manuscript was submitted on March 14, 2023; approved on October 4, 2023; published online on December 26, 2023. Discussion period open until May 26, 2024; separate discussions must be submitted for individual papers. This paper is part of the ***Journal of Geotechnical and Geoenvironmental Engineering***, © ASCE, ISSN 1090-0241.

J. Geotech. Geoenviron. Eng., 2024, 150(3): 04023141

(a)
(b)
(c)

Fig. 1. Maple Leaf Reservoir in Seattle: (a) during construction; (b) from the inside; and (c) simplified cross-sectional near the exterior wall. (Images by authors.)

this class of underground structures. Moreover, the study showed that the traditional categorization of reservoirs, as *yielding* or *unyielding*, is not adequate for the seismic design. Some numerical studies have focused on the seismic performance of buried reservoirs most of which considered a 2D representation (Harounian et al. 2014; Hudson et al. 2014; Deng et al. 2016; Zhang et al. 2017). In the seismic evaluation program of Seattle reservoirs (CH2MHILL 2015), both 2D and 3D models were carried out. Using the numerical models, the investigation program found that the existing reservoirs are seismically deficient. The reservoirs' responses were shown to be highly complex, 3D in nature, highly influenced by the inertia of the roof, and exhibit stress concentration and damage modes that cannot be captured using code-based or simplified methods. While those studies provided valuable insights, no field measurements or experimental data on the 3D FSSI of buried reservoirs are available, which makes numerical modeling approaches difficult to validate. Also, the available 2D experimental work does not include some of the important features of reservoirs such as the presence of columns, typical aspect ratios, 3D features, presence of water, and so on. Therefore, the 3D large-scale coupling between SSI systems and water has not been conclusively studied before and remains a significant challenge to engineers who often rely on simplified nonvalidated design procedures.

In this paper, the seismic FSSI of buried water reservoirs is investigated experimentally and numerically. First, two unique sets of centrifuge model tests on water reservoirs buried in dry sand were carried out. The two sets differ in the reservoir orientation with respect to the motion direction to study *pseudo* 2D motion effects. Cases with three different levels of water filling subjected to six earthquake ground motions were studied resulting in a total of 36 different combinations. Numerical simulations of the centrifuge tests were then developed using LS-DYNA: a widely available, general-purpose finite-element (FE) software package. The measured and computed results were compared in terms of accelerations, bending moment increments in the reservoir structure, and hydrodynamic pressures of the stored water and showed a satisfactory agreement. The validated numerical models were further used to gain a better understanding of the reservoir seismic response mechanism. It was found that the induced seismic stresses are not uniformly distributed, which highlights the importance of considering the 3D nature of the problem. Also, the *pseudo* 2D motion effects resulted in stress concentrations at specific locations in the reservoir, especially near the corners. The case of an empty reservoir was found to produce the highest base slippage. The results in terms of bending moment, total base shear, and roof racking showed that the full reservoir is the governing case. Therefore, not accounting for FSSI effects in such structures would underestimate the seismic demands.

Buried Water Reservoirs

Buried reservoirs have a multitude of details and configurations (Kenmir 1968; Hashash et al. 2017), and they are mostly constructed using reinforced concrete. Some examples of real reservoirs that are located on the US West Coast are listed in Table S1. The outer shell can be designed to take the form of a circular, rectangular, or irregular shape depending on several factors, including what would best fit the site. Unlike other conventional underground structures, buried reservoirs have an aspect ratio close to that of a pizza box and are often constructed at shallow depths. The exterior shell can be composed of nonprestressed or thinner prestressed concrete walls; the latter option is more often utilized for circular reservoirs. The construction of prestressed reservoirs requires extra precautions to avoid the corrosion of tensioning cables through hairline cracks. The considerable distance separating parallel exterior walls necessitates the construction of equally spaced interior columns to support the weight of the roof [Fig. 1(c)]. The roof carries a relatively thin layer of backfill and is usually composed of a flat slab with column crowns/drop-panels to prevent punching shear failure. The columns, in return, are supported on a leveled foundation slab with increased thickness near the vicinity of the columns and the walls. To control crack formation, the bottom slab is disjointed in both directions with well-sealed expansion/contraction joints commonly situated midway between the columns; resulting in what appears to be a grid within. There may or may not be intermediate divider walls depending on the size of the reservoir. To maintain the stored water quality and tolerate wave sloshing produced by earthquakes, a freeboard distance, which is the clear distance between the maximum water surface level and the roof, is provided. Beyond any differences in construction details, the configuration of underground reservoirs overall clearly differs from that of other traditional underground facilities, especially given the presence of stored water. Therefore, extending the commonly used methods of seismic analysis and design of underground structures (Wang 1993; Hashash et al. 2001) to reservoirs is unsupported by numerical or physical experiments.

Centrifuge Experimental Program

A series of centrifuge model tests, henceforth called the BRE tests (AlKhatib 2023), was performed to investigate the seismic FSSI response of a model reservoir in dry sand. Morales (2020) investigated the hydrodynamic forces acting on the interior of a rigid tank structure through a series of centrifuge model tests. Following this work, the BRE model test series was designed to expand the current understanding of system-level performance and investigate the full FSSI problem in conditions more representative of those in the field. The 24 × 24 × 8-m model reservoir structure, constructed using fabricated aluminum metal with a bolted construction design, was buried at a shallow depth within a dry deposit of medium-dense sand. The experimental program consisted of two sets—BRE-N and BRE-R—which differ in the reservoir orientation with respect to the direction of shaking to include *pseudo* 2D motion effects. Both sets subjected the buried reservoir structure to a series of broadband earthquake motions and with the enclosed water at varying levels; initially with an empty reservoir and progressing to a "full" condition that emulates typical freeboard conditions for this class of structures.

The models were tested on the large 9-m-radius centrifuge at the Center for Geotechnical Modeling (CGM) at the University of California, Davis, in the Flexible Shear Beam 2.1 (FSB2) container (Wilson et al. 1997; Boulanger et al. 2018). All information and results presented herein have been converted to prototype units unless otherwise specified. The scaling laws described by Garnier et al. (2007), listed in Table S2, detail the scaling factors applied to achieve a prototype scale response as a function of the gravitational scale factor, N, applied to the model during testing.

Test Configuration

Fig. 2 illustrates the configuration of the tests in elevation and plan view. The FSB2 container was used to perform the test series. The compromise between the dimensions of the centrifuge FSB2 container, the targeted centrifugal acceleration, and accommodating a representative buried reservoir in the test led to the decision of emulating the structural parameters of a small, buried water reservoir currently in operation. As such, the model reservoir was aimed to emulate the dimensions and structural properties of the Myrtle reservoir, constructed in Seattle (CH2MHILL 2015). Table S3 compares the model reservoir properties and the estimated Myrtle reservoir properties (CH2MHILL 2015) while Fig. S1 illustrates the materials and connection details of the model reservoir in model scale. The model reservoir was manufactured from a uniform sheet of 6061-T6 aluminum with a 4.8 mm (3/16 in.) material thickness, and it was assembled using angle sections and steel alloy socket-headed screws. Nine columns were included inside the reservoir, using 9.5 mm (3/8 in.) 6061-T6 aluminum bolts, with equal spacing of 6.1 m. A waterproofing epoxy was applied to the seams of the construction joint to ensure the reservoir would not leak during testing. Particular attention was paid to matching lateral stiffness, defined as force required to cause unit deformation of roof relative to the floor in the horizontal direction, to the value calculated from as-built designs of the Myrtle Reservoir to the extent possible. The reservoir structure was designed and checked to remain elastic throughout the entire experiment in order to reduce effects from preceding motion(s).

The entire soil profile comprised Ottawa F-65 Quartz sand, which was dry pluviated in 2.5-cm (model scale) lifts, utilizing CGM's pluviator along with a hose and a diffusing screen, to a final uniform initial relative density of $D_r \approx 65\%$. The final thickness of

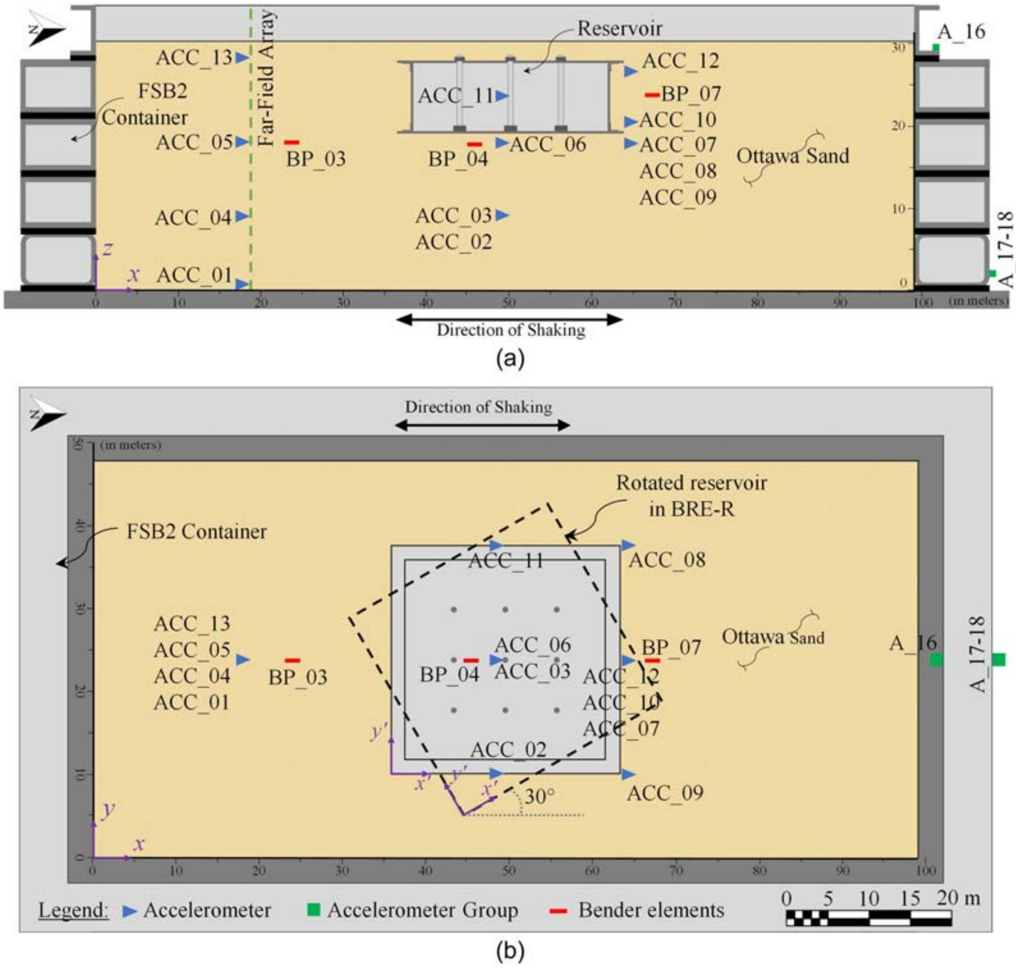

Fig. 2. Instrumentation layout of the soil and container in BRE-N: (a) elevation view; and (b) plan view.

Table 1. Properties of Ottawa F-65 sand used in the BRE test series

Test ID	Parameter	Value
BRE-N	Relative density, D_r (%)	65.0
	Void ratio, e	0.63
	Dry unit weight ($\mathrm{kN/m^3}$)	16.22
BRE-R	Relative density, D_r (%)	72.0
	Void ratio, e	0.61
	Dry unit weight ($\mathrm{kN/m^3}$)	16.42

the soil profile was 50.2 cm in model scale and ~30 m in prototype scale. Table 1 summarizes the relevant Ottawa F-65 soil properties. The soil underlying the reservoir for the BRE-N test was reused for the BRE-R test, with readings from various sensors estimating the initial relative density (D_r) for BRE-R as approximately 72%, and as such experienced limited densification during the testing sequence of BRE-N. As a result, and after the placement of the model reservoir in its rotated position, the newly dry-pluviated soil was placed at a similar relative density (72%) by using a more restrictive diffusing screen to ensure, again, an overall uniform soil profile. Cone penetration tests (CPTs) performed before shaking confirmed the uniformity of the profile as shown in Fig. S2.

The reservoir structure was buried at a shallow depth and subjected to a series of one-directional broadband earthquake motions. The depth of cover for both configurations was approximately 1.5 m. Fig. 3(a) shows BRE-N after placing the model reservoir in FSB2 and before continuing soil pluviation, while Fig. 3(b) shows the model reservoir without the roof. Both sets (BRE-N and BRE-R) were spun to 60 g (e.g., $N = 60$) at the center of the model using an angular speed of 78.7 rpm of the centrifuge container. The centrifuge at CGM is capable of producing up to 75 g of centrifugal acceleration and the chosen acceleration level (60 g) was successfully utilized in previous studies (Hushmand et al. 2016; Ng 2014). In addition, the large 9-m centrifuge radius, which is the largest radius of any centrifuge with a shake table worldwide, would limit the stress distortion of the model (Taylor 2018). The first sequence of shaking was performed on an empty reservoir structure, while subsequent shaking sequences were performed on the same structure while increasing the water depth inside of the reservoir in flight. BRE-R used the same reservoir structure and testing sequence, but with the model reservoir rotated by 30° with respect to the direction of shaking to capture the effects of a bidirectional earthquake motion.

Model Instrumentation

The model structure was instrumented with strain gauges, accelerometers, and tactile pressure sensors at key locations that would provide complete tracking of the structural response and the development of water and soil pressures on the walls. The surrounding soil was instrumented with accelerometers and linear potentiometers (at the surface) to track accelerations, stress–strain responses, and soil settlements. Figs. 2 and 4 show the instrumentation used

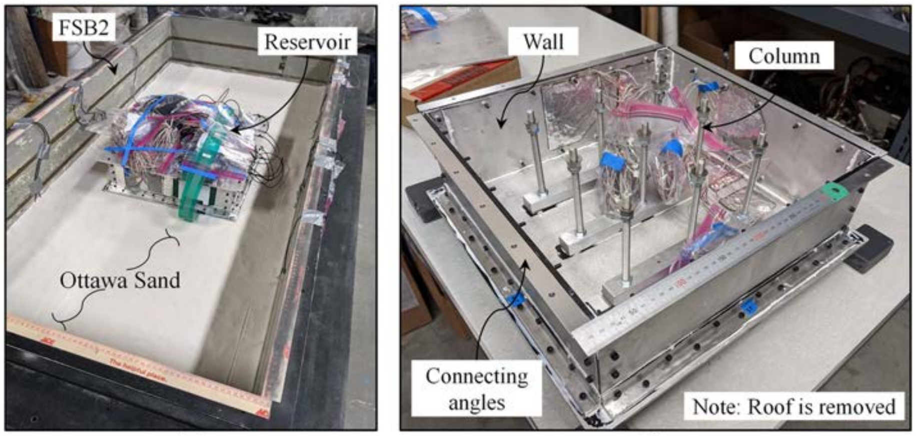

(a) (b)

Fig. 3. Pictures of (a) BRE01 test setup prior to complete reservoir burying; and (b) the reservoir.

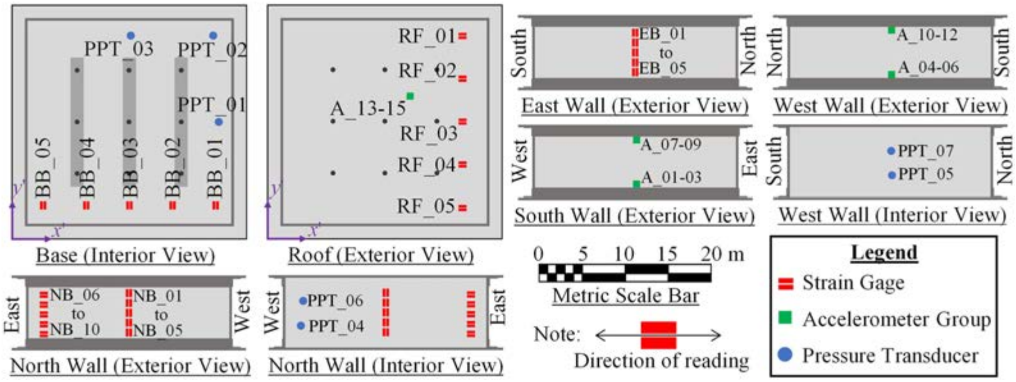

Fig. 4. Instrumentation layout of the reservoir for both BRE-N and BRE-R.

in the centrifuge model tests. Accelerometers, pore pressure transducers, strain gauges, linear potentiometers, and tactile pressure sensors were placed at key locations in the soil, on the model reservoir, and on the FSB2 container to continuously track the state and response of the model components as well as the imposed demands. Images of select sensor types used in the model are shown in Fig. S3. Challenges were encountered when attempting to obtain readings from the tactile pressure sensors in both tests, as the tabs became dislodged from the handles during shaking.

Epoxy-coated ICP accelerometers (ACC) were placed in key locations throughout the soil. An accelerometer array placed in the far field was used to measure the soil's response to the sequence of broadband motions. Other accelerometers were placed surrounding the model reservoir to capture any effects of the FSSI response. Several ICP accelerometers were also fixed to the FSB2 container to measure the container response both in the direction of shaking and placed vertically to measure any rocking. The centrifuge one-dimensional (1D) shaker was instrumented with accelerometers on the east and west side to measure achieved accelerations, and the average of the two recordings was considered the achieved input acceleration. A series of three-component accelerometer arrays were fixed to the reservoir structure (Fig. 4). These arrays were placed on the south and west model reservoir walls at the bottom and top of the wall to capture the structure's dynamic response. Previous numerical studies of buried storage reservoirs (Cheng et al. 2017) have shown that the inertia of the roof component is particularly influential on the overall seismic response of the structure, and, as such, a single 3D array was fixed to the roof of the model reservoir.

Pore pressure transducers of two types were prepared according to the procedure specified by Sinha et al. (2021) and placed inside the reservoir (Fig. 4) to record water pressures during testing. Multiple coatings of adhesive were used to ensure proper performance of the sensors throughout the rigorous testing schedule. Only one pressure transducer, PPT_03, failed during the BRE-R test.

Strain gauges were installed on the reservoir parts to record the dynamic bending strains experienced by the reservoir. The gauges had dimensions of 10.5×3.9 mm and a nominal gauge factor of 2.05, and they were all installed in a full bridge bending configuration, meaning a total of four gauges were installed at each point of interest; two gauges were installed in parallel on both sides of the reservoir part. The gauges were bonded using Loctite 496 cold-curing strain gauge adhesive, while a series of gauge protection materials were used to ensure there were no failures due to water or soil damage. Strain gauge protective coatings were applied equally on the interior and exterior wall faces to preserve measurement consistency. Individual bending strain tests performed at the CGM confirmed that the nominal sensitivity of the gauges was acceptable to record accurate measurements during testing. It wasn't feasible to install stain gauges very close to the wall base because of the bolted L-shaped angles.

Linear potentiometers (LP) were used to measure vertical displacements of the soil surface and the reservoir roof during testing. A total of five 7.6 cm (3 in.) LPs were used during testing. For both tests, the LPs were placed as follows: above the far-field soil, above the reservoir soil, attached to the northeast reservoir corner, attached to the northwest reservoir corner, and attached to the centerline of the southern edge of the reservoir roof. All LPs were fixed to mounted rigid racks placed across the top of the FSB2 container. The readings from the LPs were found not to be reliable; therefore, they were not used in this study.

Bender element shear wave velocity measurements and CPTs were performed in flight to capture the state of the soil profile and track any changes in the soil stiffness at select instants throughout the testing sequence. Soil shear wave velocities were measured after shaking events using bender elements manufactured at the CGM. Each bender element is a two-layer piezoelectric transducer (Montoya et al. 2012) coated in xylene polyurethane for abrasion resistance. Three sensor pairs consisting of one sender element and one receiver element were placed at the locations shown in Fig. 2. The sending element triggers a nondestructive shear wave pulse at the triggering time that is captured by the receiving bender element. The difference between trigger time and the receiver recognizing the signal is the response time of the recording, taking the known placement distance and dividing by the response time of the recording results in the velocity of the shear wave through the soil. The bender elements were concentrated at relatively shallow depths and in close proximity to the reservoir where the primary focus of this study is. The 6-mm (model scale) Liquefaction Experiments and Analysis Projects' (LEAP-2017) design (Carey et al. 2018) cone penetrometer with a 2,224 N (500 lbf) load cell was also used during the BRE series of centrifuge tests. The probe was pushed with a hydraulic actuator at a constant rate of 1 cm/s to a maximum depth of approximately 45.7 cm (18 in.) model scale. The measurements were baseline corrected to start from zero for each motion to eliminate any residuals carried over from the previous motion(s).

Testing Sequence and Input Motions

The testing sequence for the BRE-N and BRE-R centrifuge tests relied on filling the model reservoir with a specific volume of water in flight. In previous applications (Morales 2020), water filling on the centrifuge arm during testing was achieved by turning on a water faucet and estimating the inconsistent volumetric flow into the container. For BRE-N and BRE-R, two tanks were installed on top of the centrifuge arm to allow researchers to control the volume of water released into their centrifuge model. The two tanks were connected to a split valve and a single hose that leads into the reservoir model. The tanks were filled with approximately 9,000 cm^3 (model scale) each, representing the volume of water to fill half of the reservoir, and released after the first and second shaking sequences for each test.

The testing series was performed over a total duration of three spinning days with the tank always starting empty (BRE-N-E, BRE-R-E). After spinning up to 60 g, a CPT push (not equipped with seismic sounding) and shear wave velocity measurements using bender elements were performed, followed by a step wave motion to initiate and test the centrifuge shaker. Then, the suite of six 1D ground motions, listed in Table 2 and presented in Fig. S4 as achieved base spectral accelerations, was sequentially applied with intermittent bender element measurements of shear velocity to track the state of the soil. The same testing sequence of model characterization (CPT pushes and bender element testing for shear wave velocity) was repeated for the tank half-full (BRE-N-HF, BRE-N-HF) and full (BRE-N-F, BRE-R-F). Although the waveforms were the same, the earthquake sequence applied to the BRE-R model was a 130% scaled version of the sequence used in the BRE-N test. Increases to the BRE-R amplification factors aimed to preserve the intensity of the motions in the x' direction of the model reservoir itself (Fig. 2) when compared to the BRE-N motions while increasing the demands in the y' direction thus approaching a closer representation of the added 2D motion effects. Despite the rotation of the reservoir in BRE-R, the out-of-plane displacement of FSB2 container in y direction was limited because (1) the center of mass of the entire setup remains at the center of the container, mitigating torsional effects, and (2) the container has a significantly greater mass and natural period compared to the reservoir, effectively limiting the influence of the reservoir on the container's movement. Table 3 summarizes the

Table 2. Earthquake recordings used in the centrifuge experiments

Event	Year	M_w	Mechanism	Station	Motion ID	V_{30} (m/s)	PGA (g)	Arias (m/s)	$D_{5\text{-}95}$ (s)
Landers	1992	7.4	Strike Slip	Joshua Tree	JOS090[a]	379.32	0.27	2.30	27.10
Loma Prieta	1989	6.9	Reverse Oblique	Santa Cruz Obser.	LOB090	713.59	0.62	2.70	9.70
Northridge	1994	6.7	Reverse	Newhall W Pico	WPI046	285.93	0.65	1.50	8.80
Kobe	1995	6.9	Strike Slip	Takatori	TAK090	256.00	0.46	8.70	11.30
Tohoku	2011	9.0	Megathrust	IWT008	IWT008	~1,086	0.12	0.35	41.67

[a] A scaled version (scale factor = 1/4) of this motion is also used (JOS090R).

Table 3. Centrifuge tests configurations in model scale (prototype scale dimensions reported in parentheses in m)

Test ID	D_r (%)	Water height (cm) -E	-HF	-F	Reservoir orientation[a] (degrees)
BRE-N	65	No water	6.5 (3.9)	10.8 (7.5)	0
BRE-R	72	No water	6.5 (3.9)	10.8 (7.5)	30

[a] Counterclockwise with respect to the x-axis.

total of the six model configurations tested which, combined with the six imposed ground motions, yield a total of 36 cases.

Numerical Model Development

The centrifuge experiments were numerically reproduced using the explicit solver of LS-DYNA R11.2.0 (LSTC 2020), a general-purpose FE software. The 3D numerical models represented the prototype scale and included the following components involved in the experiments: the FSB2 container, Ottawa sand, the reservoir structure, and the stored water as shown in Fig. 5. For BRE-N, only half of the model was represented due to symmetry. Separate numerical simulations were carried out for each individual case.

The FSB2 container was designed and used in the centrifuge experiments at CGM to reduce the boundary effects that are typically encountered with rigid containers (Boulanger et al. 2018). However, the difference in the stiffness and the natural period between the container and the soil profile implies that some boundary effects can still be present. To capture these effects, an idealized representation of the FSB2 container was explicitly included in the models using eight-node solid elements. Meshing the hollow sections of the metal rings would have resulted in small mesh elements that significantly decrease the timestep, and thus increase the simulation runtime when using the explicit solver. Therefore, it was decided to idealize the hollow sections as rigid solid sections with equivalent densities (ρ). The adequacy of the idealization was confirmed through separate implicit eigenvalue analyses of the original and the idealized containers in which the eigenvalues and eigenvectors were found to be similar. The in-between rubber rings were modeled using elastic brick elements with Poisson's ratio $(\nu) = 0.49$. The section and material properties of the FSB2 metal rings and rubber layers are listed in Table S4. The interface between the soil and the container was modeled using a surface-to-surface penalty-based contact algorithm available in LS-DYNA that allows sliding and gapping to occur. This interface follows the Coulomb friction law with a friction coefficient equal to two-thirds of that of the soil.

The uniform Ottawa sand soil profile in the numerical simulations was modeled using eight-node constant stress solid elements with hourglass control, and was divided into layers to allow for maximum shear wave frequency propagation $f_{\max}$ of at least 30 Hz, such that

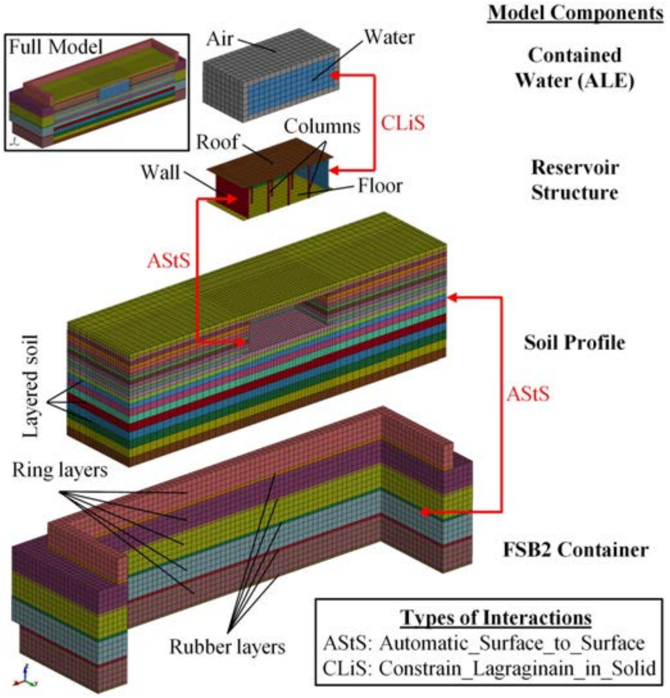

Fig. 5. Exploded view showing the FE model components (for BRE-N).

$$f_{\max} = \frac{V_s}{4h} \geq 30\ \text{Hz} \tag{1}$$

where V_s and h are the initial shear wave velocity and height of the soil layer, respectively. The initial shear wave velocity and friction angle ϕ for each layer were obtained using the formulations proposed by Menq (2003) and Bolton (1986), respectively. The shear wave velocity and friction angle profiles that were used to derive the shear modulus reduction and damping curves for BRE-N and BRE-R are presented in Fig. 6 along with the bender element measurements that were taken before, during, and after the shaking sequence. Pressure-dependent shear modulus reduction and damping curves for each soil layer were generated following the formulation proposed by Darendeli (2001) and then corrected to reach 95% of the shear strength at 10% shear strain according to the General Quadratic/Hyperbolic model proposed by Groholski et al. (2016). The newly developed constitutive model, I-soil, was used and implemented in LS-DYNA as a user-defined material model (Numanoglu et al. 2023). I-soil is a 3D effective stress soil model built upon the distributed element plasticity framework

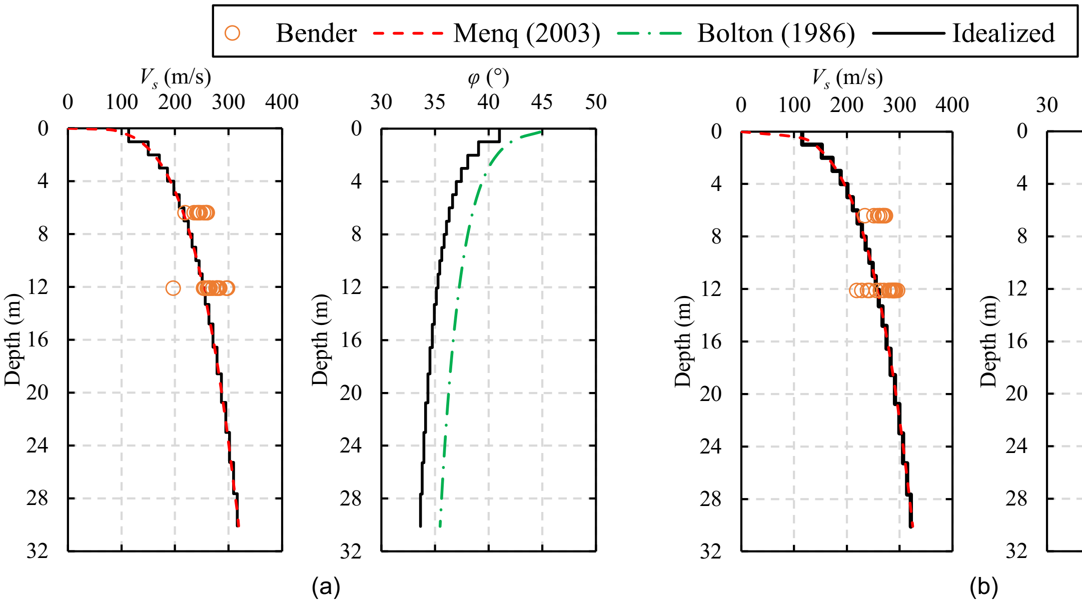

(a)

(b)

Fig. 6. Shear wave velocity and friction angle distributions with depth for (a) BRE-N; and (b) BRE-R.

introduced by Iwan (1967) and extended by Chiang and Beck (1994). The model describes small-strain nonlinearity in terms of modulus reduction, hysteretic damping, effective mean stress-dependent shear stress–shear strain behavior, and shear-induced volumetric behavior in terms of strains and porewater pressure in 3D stress space using 30 Drucker–Prager-type conical yield surfaces. A non-Masing un/reloading hysteresis formulation developed by Phillips and Hashash (2009) and generalized to 3D by Numanoglu et al. (2017) was used to better represent soil damping, which would otherwise be significantly overestimated when using Masing rules, especially at large strains. The strength and stiffness pressure-dependency along with the shear-induced volumetric response were used in the material model while using recommended values for the corresponding parameters as provided in Table 4.

The aluminum reservoir structure was modeled using four-node fully integrated shell elements for the floor, roof, and walls, and two-node Hughes–Liu beam elements with cross-sectional integration for the columns. The effective area of the bolts was considered for the columns' cross-sectional area. The reservoir structure was designed to behave elastically under multiple shaking events without yielding, which was further confirmed in the subsequent analyses. As such, all structural elements were modeled using the linear elastic material model with $\rho = 2{,}713\ \mathrm{kg/m^3}$, Young's modulus $(E) = 69$ GPa, and $\nu = 0.33$. Two through-thickness integration points were used for the shell and beam elements. Similar to the container–soil contact, the contact between the reservoir and the surrounding soil was modeled using a surface–surface contract algorithm that solves for both normal and frictional forces.

Table 4. Input parameters for the soil material model

Parameter	Value
Darendeli (2001)	
At-rest lateral earth pressure coefficient, K_o	0.4
Plasticity index, PI	0
Over-consolidation ratio, OCR	1
Loading frequency[a]	1
Number of loading cycles[a]	10
I-soil (Numanoglu et al. 2017)	
Poisson's ratio, ν	0.3
Cut-off pressure, σ_0' (kPa)	−1
Stiffness PD coefficient, b	0.5
Strength PD parameters a_0, a_1, a_2	0, 0, 1
Volumetric strains parameters η_{dsr}, A_0[a]	0.51, 0.4

[a] Recommended values.

The Arbitrary Lagrangian-Eulerian (ALE) formulation was used to model the stored water. ALE is a computational system that is neither attached to the material (Lagrangian-type FE formulation) nor fixed in space (Eulerian-type FE formulation). Therefore, it resolves many of the shortcomings that the traditional Lagrangian- and Eulerian-type FE simulations have. For more details on the ALE formulation, the reader can refer to the study by AlKhatib (2023) where the ALE formulation was validated and tested against experimental measurements, as the first step of this project, and was found to well-represent the water dynamic behavior. The Grüneisen equation of state was used to describe the water material with the material properties listed in Table 5. The interface between the reservoir shell and the water was established using a coupling feature available in LS-DYNA. The coupling prevents the water from penetrating the reservoir structure by applying counter normal forces while allowing slippage. To have accurate readings of water pressures at points of interest, an automatic mesh motion that follows the reservoir movement was activated for the ALE background mesh.

The base of the model (at the bottom level of the FSB2 container) was fixed in all directions except for the x-direction in which

Table 5. Water material properties and related Grüneisen EOS parameters

Category	Variable	Value
Material properties	Density (kg/m^3)	1,000
	Dynamic viscosity (Pa · s)	8.9×10^{-04}
Grüneisen EOS parameters	C (m/s)	1,647
	S_1	1.921
	S_2	0.096
	S_3	0
	γ_0	0.35
	a	0

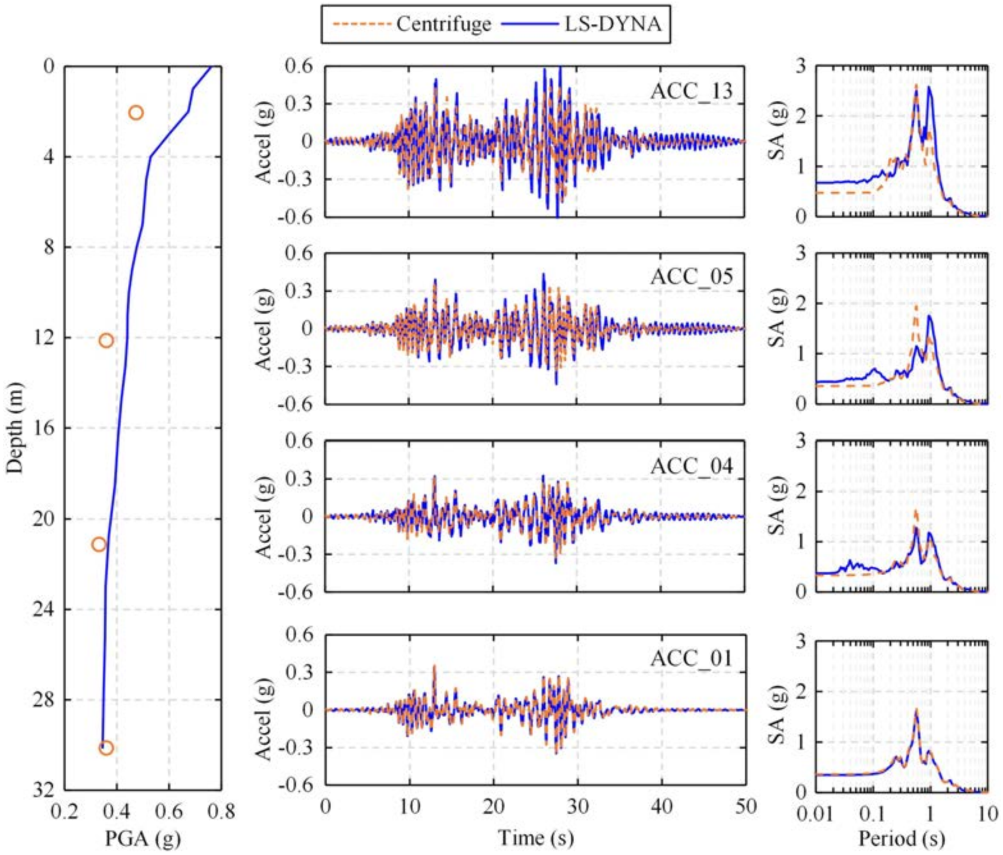

Fig. 7. Acceleration at the far-field array in BRE-R-E under LOB090.

the achieved 1D motion was applied. The achieved motion was applied as a prescribed acceleration time history, and the model was subjected to a constant downward gravitational acceleration of 9.81 $\mathrm{m/s^2}$ throughout the simulation. The soil (except at the container base) and the reservoir (along with the water inside it) were free to move in all three directions including vertical settlement. Damping was applied to the container rubber layers, the soil layers, and the reservoir structure using a frequency-independent formulation with frequencies ranging from 0.1 to 30 Hz. The range of frequencies was chosen such that it covers the frequencies imposed by the base motion while keeping a ratio of $F_{\mathrm{high}}/F_{\mathrm{low}} \leq 300$, as suggested by the LS-DYNA manual (LSTC 2020). All reservoir structural parts were assigned a 2% damping ratio, whereas the container rubber layers were assigned an 8% damping ratio. The small-strain damping ratio for each soil layer was obtained from the Darendeli (2001) formulation (i.e., D_{min}).

Numerical Simulation Results of Experiments

The simulation results were compared to the experimental measurements in terms of (1) soil far-field and near-field accelerations, (2) FSB2 container accelerations, (3) reservoir structure accelerations, (4) bending moment increments in the reservoir structure, and (5) hydrodynamic pressures of the stored water.

The evaluation started with the far-field site response using a far-field array composed of four accelerometers located at the mid-distance between the container and the reservoir, as shown in Fig. 2. The intent was to assess the performance of the soil model in capturing the site response at a location that is expected to experience minimal influence from the interaction with the container and the reservoir structures. The numerical results showed a good agreement in capturing the measured variation of PGA with depth as well as reasonably matching the acceleration time series and their corresponding (5% damped) response spectrum recorded by the four sensors. As an example, Fig. 7 shows a comparison of the measured and the computed accelerations at the far-field array in BRE-R-E under the LOB090 motion. Moreover, Figs. S5 and S6 show examples of near-field soil accelerations and reservoir accelerations, respectively. In Fig. S6(a), the accelerations are shown to be primarily in the x'-direction for the case of BRE-N. On the other hand, in the case of BRE-R, accelerations can be computed in both the x'-and y'-directions due to the reservoir being at an angle to the direction of motion, as illustrated in Fig. S6(b), emulating a 2D motion with respect to the reservoir. The numerical model was able to capture the reservoir reaction to shaking in both cases. Two accelerometers located on the bottom and the top rings of FSB2 were used to evaluate the container's response to shaking. An example of the computed and measured acceleration and response spectrum is presented in Fig. S7.

Fig. 8 shows water pressures measured compared to the ALE pressures computed by LS-DYNA for the case of BRE-N-F under JOS090 motion. As expected, the hydrodynamic pressures are highest near the north and south walls and are well captured by the model.

The measured bending strain increments were not baseline corrected in order to capture potential permanent changes. The measured and computed maximum and minimum bending moment increments (ΔM) at the center of the north wall (NB_01-05) for all cases are summarized in Fig. 9. Under an elastic state, the bending moment (M) can be related to the bending strain (ε_b) as

$$M = ES\varepsilon_b \tag{2}$$

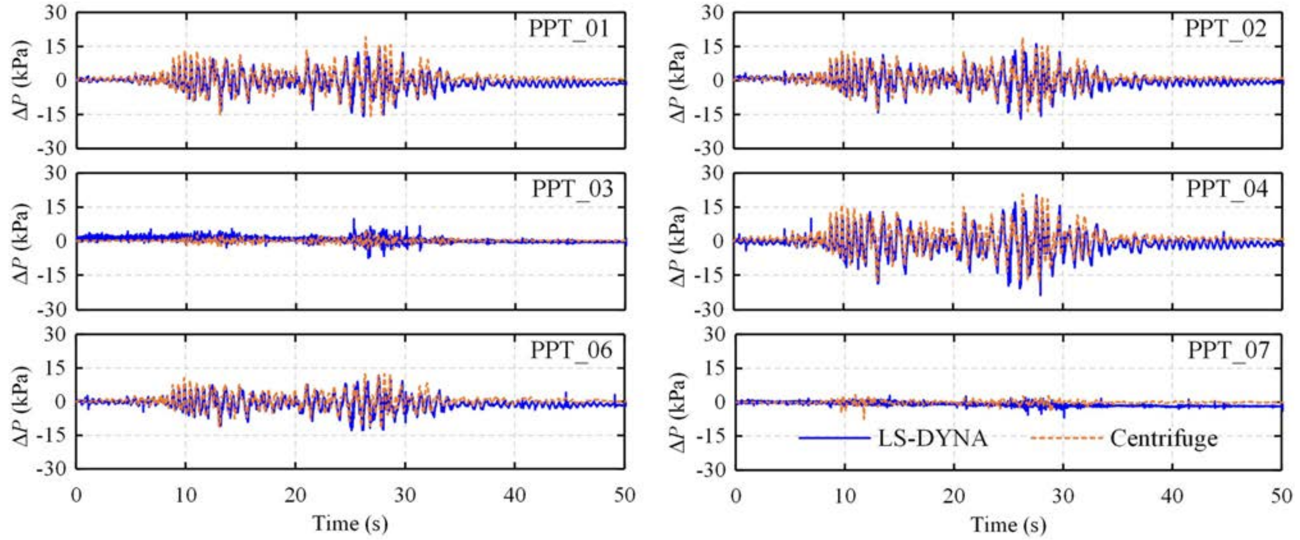

Fig. 8. Dynamic water pressures in BRE-N-F under JOS090.

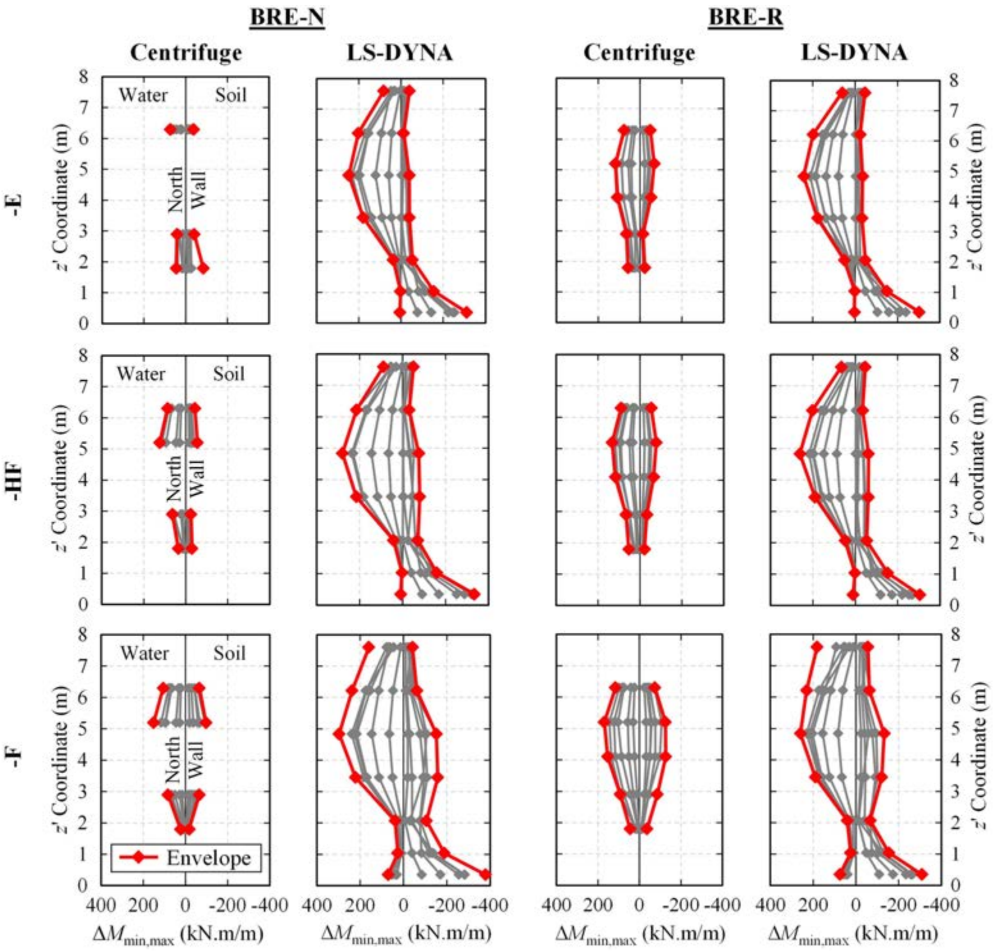

Fig. 9. Range of dynamic moment increments at the north wall (sensors NB_01-05) for all motions in BRE-N.

where S is the section modulus. The experimental and numerical results share the same distribution pattern and order of magnitude.

The same reasonable agreement between the measured response and the numerical counterpart is observed for the other configurations and motions. Summary plots of the log residual spectral accelerations are presented in Fig. 10, where the log residual is defined as

$$\text{Residual}\, X = \log\left(\frac{X_{\text{measured}}}{X_{\text{computed}}}\right) \tag{3}$$

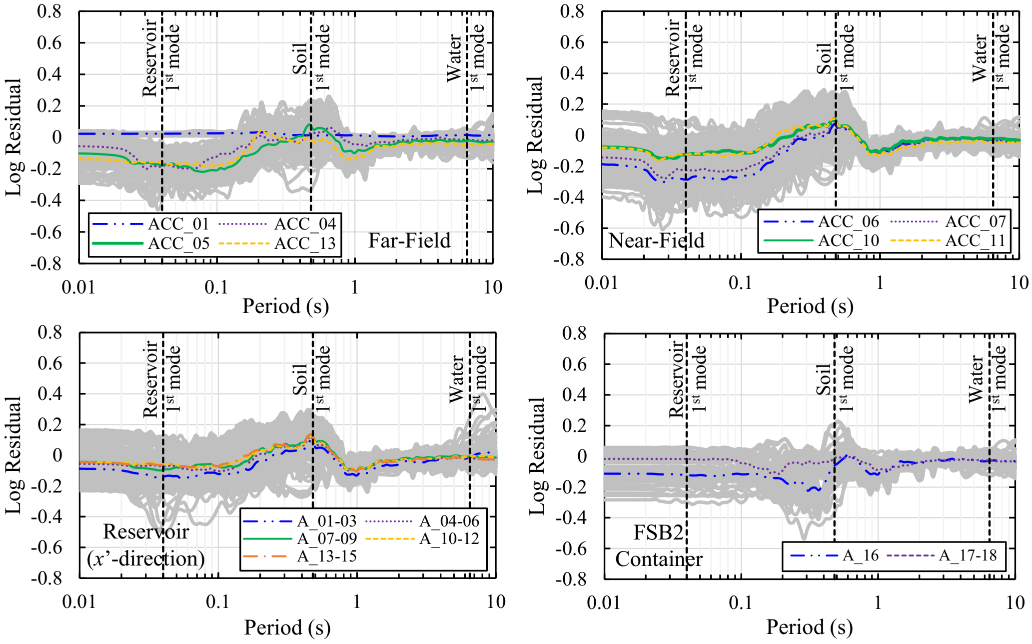

Fig. 10. Log residual of the computed 5% damped spectral acceleration. Lines highlighted in the legend indicate the average for each sensor.

A residual greater than zero indicates an underestimation while a residual less than zero indicates an overestimation. It was observed that the numerical model tended to overestimate the high frequencies (low periods) of the measured spectral acceleration. This mismatch could likely be attributed to the high frequency filtering applied during the data processing stage of the centrifuge measurements. Like other centrifuge experiments, data processing/filtering is a necessary stage to remove the inevitable artificial noise encountered during the experiment. In contrast, the results obtained from the numerical models were not filtered or modified. Consequently, unlike the numerical results, the measurements exhibit a consistent "flatness" in the spectral acceleration at low periods (<0.1 s) as an indication of the applied filtering (Fig. 7). However, a better agreement between the measured and predicted spectral acceleration was observed at medium to low frequencies (medium to high periods), as demonstrated in Fig. 10.

Discussion

As demonstrated in the previous section, the numerical models showed a good performance in reasonably reproducing the outcome of the centrifuge experiments. In what follows, a discussion is presented on the reservoir FSSI response mechanism when subjected to shaking. The numerical data were best utilized to fill in the gaps for the locations or response variables that were missed or otherwise difficult to measure during the experiments; hence, LS-DYNA models served as a very useful complementary tool in the investigation.

Hydrodynamic Response

In general, water dynamic pressures can be broadly separated into impulsive and convective parts (Housner 1957). The impulsive pressures are associated with the inertial forces produced by the impulsive mass of water which is firmly attached to the container; making the pressures generated directly proportional to the container acceleration. On the other hand, the convective pressures are generated from water sloshing taking place near the free surface and as such can continue to exist after the end of motion until the sloshing is damped out. The significance of convective pressures depends on the spectral accelerations at the water's natural periods. Reservoirs are typically characterized by long horizontal dimensions and relatively shallow depths, which translate to long natural water periods (>10 s). Looking to the fact that the wide range of earthquakes is associated with low spectral accelerations at high periods, impulsive pressures often dominate. This can be observed through the example shown in Fig. 8 where the pressure time series is proportional to that of the reservoir acceleration and almost no dynamic pressures are observed after the end of shaking.

The measured and computed normalized peak dynamic pressures, defined as $\max|P - P_o|/P_o$, at the north wall near the northwest corner (e.g., PPT_04 and _06) in the function of reservoir peak x' acceleration are presented in Fig. 11. Results from centrifuge model tests of hydrodynamic pressures in rigid tanks under 1D motions by Morales (2020), referred to as HYE, are superimposed for comparison. As shown in Fig. 11(a), the measurements from BRE-N were observed to be mostly in line with the results of HYE, because both were subjected to 1D shaking and the reservoir was evaluated to be relatively stiff (Table S3). However, BRE-R consistently recorded lower pressures than both BRE-N and HYE. To understand why that is the case, a similar plot for the computed response is presented in Fig. 11(b) which agrees with the measured responses. Yet, complementary results near the southwest corner were added and showed higher pressures when compared to all the other cases. The main reason for this is because of the constant orientation of the *pseudo* 2D motion with respect to the reservoir. When projecting the resultant motion on the four walls, as shown with the small arrows near corners in Fig. 11(b), one can find that two quadrants of the reservoir that are along the direction of shaking would experience constructive interference in which the two adjacent walls would push in or pull out concurrently, thus amplifying the pressures. The other two quadrants, which PPT_04 and _06 fall under, would experience destructive interference; yielding lower pressures than the case with 1D motion (e.g., BRE-N and HYE). This implies that considering the 2D motion would result in nonuniform distribution of hydrodynamic pressures.

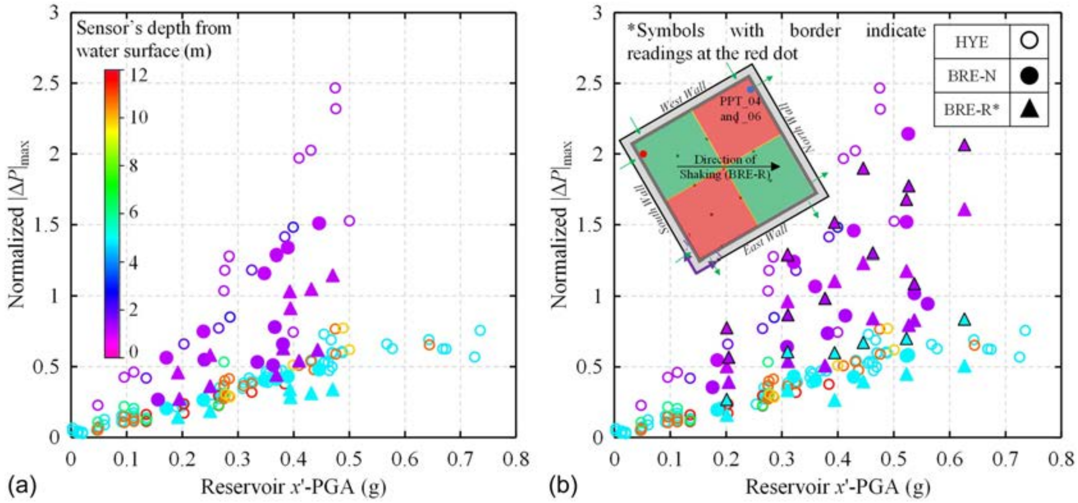

Fig. 11. Plots of distribution of the normalized peak pressures at the north wall (sensors PPT_04 and _06): (a) measured distribution; and (b) computed distribution. Results from HYE experiments are superimposed. (Data from Morales 2020.)

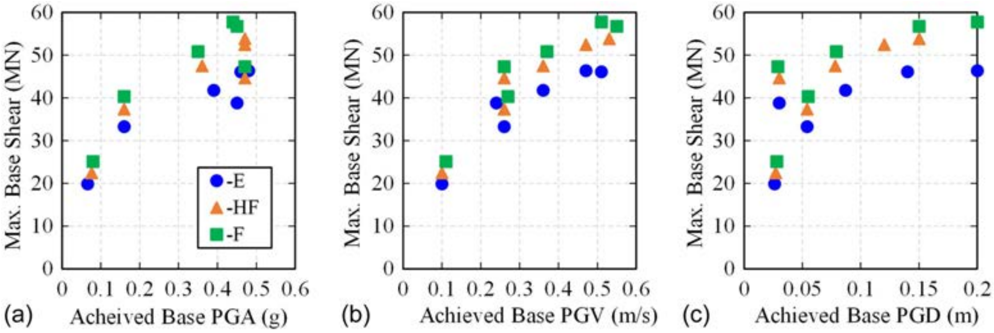

Fig. 12. Computed reservoir maximum base shear (for BRE-N) against achieved: (a) PGA; (b) PGV; and (c) PGD.

Reservoir Structural Response

Reservoir response can be evaluated by looking at the behavior of the individual structural elements and the structural system as a whole. The evaluation started by computing the total base shear. The total base shear represents the total lateral force imparted on the structure during shaking and is defined as the sum of all shear forces generated in the vertical elements just above the base slab. The total base shear was then divided into the different structural elements to observe the seismic demand distribution. In terms of deformations, the base slippage, defined as the relative movement of the base slab with respect to the underlying soil, was computed along with the roof racking shape and magnitude. The vertical moment and effective stress distribution on the walls were evaluated as well.

Fig. 12 presents the change in the computed maximum total base shear with respect to the achieved peak motion characteristics for BRE-N: peak ground acceleration (PGA), peak ground velocity (PGV), and peak ground displacement (PGD). As expected, the total base shear is shown to increase with increasing intensity measures. However, a nonlinear trend can be observed which can be mainly attributed to soil material nonlinearity. The case of the full reservoir (BRE-N-F) is observed to result in the highest base shear with an increase of up to 25% compared to the empty case (BRE-N-E). To investigate why the full reservoir is the governing scenario, results from the numerical models are used. It was found that, on either side of the reservoir, the changes in the lateral pressures exerted by the retained soil and the stored water are opposite. To demonstrate this, Fig. S8 shows the computed soil and water total force induced on the north and south walls for the case of BRE-N-F under WPI046 motion. It shows that as the soil lateral earth pressure increases the water pressure decreases and vice versa. This would result in the overall amplification in the base shear.

The lateral resisting structural elements can be broadly divided into three groups: (1) the walls parallel to the motion (e.g., east and west walls in BRE-N), (2) the walls perpendicular to the motion (e.g., north and south walls in BRE-N), and (3) the columns. In Fig. 13, the total base shear is further disaggregated into the three resisting groups. The roof slab acts as a diaphragm that transmits, primarily through in-plane shear, the lateral forces to the different resisting elements. The relative stiffnesses of the different resisting elements govern the distribution of the lateral forces on those elements. Therefore, the columns showed very little resistance, while the walls parallel to the motion showed the greatest.

Base slippage may occur during earthquakes when the shear forces transmitted between the underlying soil and the reservoir base exceed the friction capacity at the interface. Fig. 14 presents the base slippage of the reservoir in the three cases of water filling. At low PGA (<0.2 g), no slippage was encountered in the three cases. The slippage in full and half-full cases only occurred at PGAs >0.35 g. As the PGA increased, the slippage magnitude

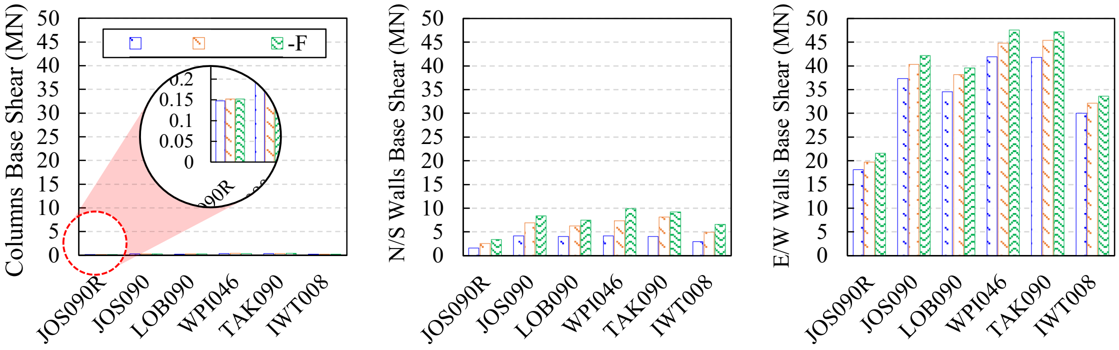

(a) (b) (c)

Fig. 13. Computed base shear of (a) columns; (b) north and south walls; and (c) east and west walls in BRE-N.

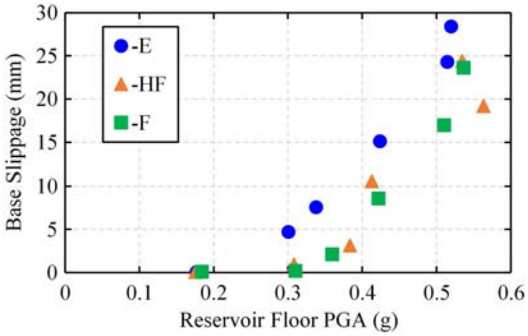

Fig. 14. Computed base slippage as a function of reservoir PGA in BRE-N.

increased with the case of the empty reservoir yielding the highest values. The reason for this is that the weight of water increases the normal stress on the underlying soil, thus increasing the frictional capacity and reducing the base slippage.

Fig. 9 shows a vertical distribution of moments being quite different than what was recorded in previous centrifuge experiments of underground excavations or buried structures (Hashash et al. 2018) most of which can be categorized either as a cantilever (Al Atik and Sitar 2010), a moment-resisting frame (Hushmand et al. 2016), or other 2D lateral resisting system. In the case of reservoirs, the distribution suggests a wall that is partially fixed, rotationally and translationally, from both ends. That is because the slab acts as a diaphragm that transmits the lateral forces to the adjacent east and west walls (e.g., shear walls). Therefore, this suggests that the lateral resisting nature of reservoirs is 3D. The higher moments near the base were attributed to the higher rotational stiffness (resulting from soil bearing against the reservoir base and footing) and translational stiffness (due to friction with the soil) of the bottom connection compared to the top connection.

Fig. S9 presents the computed total moment (sum of static and dynamic moments) version of Fig. 9, because it is a more relevant variable to be considered in the design. At static conditions and before ground motion started, the empty case showed the highest moment demands, and the full case showed the lowest. The water pressures acting on the inside face of the wall would partly counteract the earth pressures acting on the outside face, thus reducing the demands. However, during shaking, the range of total moment generated in the full case overcame that of the other two cases, as also shown in Fig. 9. Notably, due to the hydrodynamic pressures, a reverse in moment sign (e.g., negative moment) was encountered at the midheight of the wall; suggesting that the presence of water may result in tension cracking to occur on both sides of the wall.

Racking deformation, sometimes referred to as ovaling for circular shape tunnels, is a widely used parameter in the seismic design of underground structures (Hashash et al. 2001). It is defined as the relative transverse displacement between the top and bottom of the structure. The structural racking stiffness is the ratio of lateral force over relative displacement. For most underground structures the racking deformation is assumed to be uniform across the axis of the structure due to the uniformity in racking stiffness. Fig. 15 presents the racking shape of the roof in BRE-N along a cross section from the east to the west wall passing through the center of the reservoir. It can be noticed that the racking deformation is not uniform and is taking a parabolic shape. It is lowest at the walls,

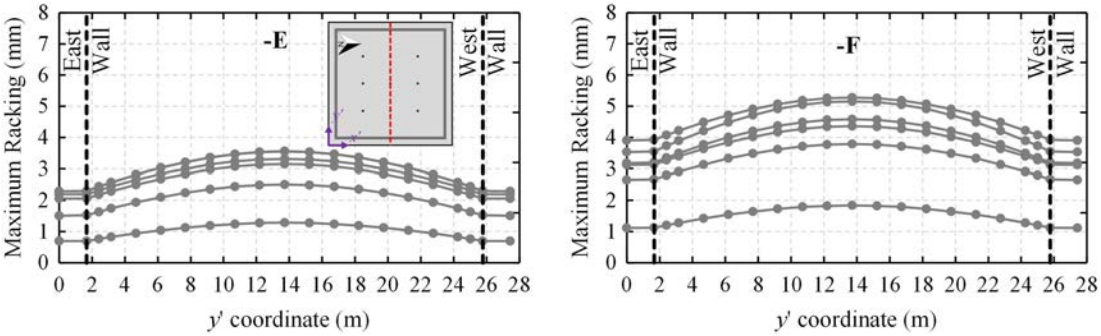

Fig. 15. Computed roof racking in the direction of shaking at a section cutting through $x' = 14$ m in BRE-N.

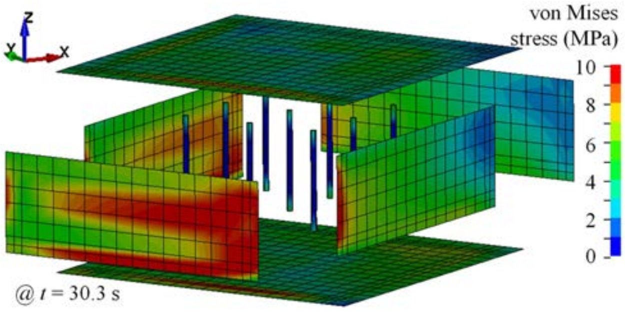

Fig. 16. Computed von Mises stress contour in the reservoir structure in BRE-R-F under JOS090 (exploded view).

where the racking stiffness is high and increases as moving away from the walls, peaking at the center. The racking deformations were observed to amplify in the case of the full reservoir due to water-induced pressures as already discussed.

The unique shape and configuration of buried reservoirs, in addition to the presence of water, make it challenging to analytically assess the stress distribution inside the structure during an earthquake. An example is presented in Fig. 16, which shows the von Mises stress distribution in the reservoir structure in BRE-R-F under JOS090 motion. The stress is seen to be nonuniformly distributed and concentrated toward the corners. The effect of *pseudo* 2D motion was observed to increase the demands especially at the corners as seen in Fig. 17, which compares the stress demands of BRE-N against that of BRE-R at different locations in the reservoir. In 2D motions, the seismic demands accumulated from both directions into the stiff zone at the corners causing stress there to increase. This shows that the seismic behavior of the reservoir is 3D and that the demands may be underestimated, particularly at the corners, if only 1D motion is taken into account.

Earth Pressure Response

The computed earth pressures obtained from the FE models are presented in Fig. 18. Fig. 18(a) shows the maximum vertical distribution of the total earth pressures computed before, during, and after shaking at the middle of the north wall. The initial static pressures fall mostly between the at-rest, $K_o = 1 - \sin\phi$, and the active, $K_A = \tan^2(45 - \phi/2)$, earth pressure lines. During shaking, the pressures are seen to fall in the range of the Mononobe–Okabe (M-O) solution (Okabe 1924) at the midheight where the wall is most flexible. However, they are higher at the top near the supporting slab, and at the bottom, partly due to base slippage. After the end-of-motion, a permanent increase in earth pressures is observed owing to the shake-induced densification of soil. The occurrence of the densification was verified by the increase in the relative density recorded from start to end of BRE-N (from 65% to 72%). Fig. 18(b) presents the horizontal distribution of the dynamic earth pressures at the midheight of the north wall. The pressures greatly increased near the corners, which can be attributed to the arching effect where the stresses are attracted to the stiff region at the corners. Fig. 18(c) compares the dynamic coefficient of lateral earth pressure, ΔK_E, back-calculated from the FE models against the M-O solution for yielding walls and the Wood (1973) solution for unyielding walls. ΔK_E was originally proposed by Seed and Whitman (1970) assuming an equivalent triangular distribution of dynamic lateral earth pressures. ΔK_E was back-calculated for the FE models by dividing the maximum dynamic force (per unit width) by $\gamma H^2/2$, where γ is the total unit weight of soil and H is the wall height. In the middle of the wall, the results fall in between the M-O and Wood solutions. Yet, at the corner, ΔK_E is higher than predicted by either of the methods due to the arching effect, which is not considered by the analytical solutions.

Conclusions and Implications

The seismic FSSI response of buried water reservoirs was studied through centrifuge model testing and advanced FE numerical modeling. The experimental program consisted of two sets— BRE-N and BRE-R—that differ in the reservoir orientation with respect to the motion direction. Both sets subjected the buried reservoir to broadband earthquake motions at varying interior water levels; initially with an empty reservoir and progressing to a "full" condition. The produced data set included a total number of 36 cases. Numerical simulations were then developed using LS-DYNA to reproduce the experiments. Accelerations of the container, the near- and far-field soil, and the reservoir structure obtained from the experiments and the FE models were in good agreement. The computed and measured incremental bending moments in the reservoir structure showed a reasonable match, and the measured changes in the water pressures were well-captured by the numerical models for both cases of half-full and full reservoirs. The validated numerical models were further used to have a more in-depth evaluation by having access to data that are not measured in the experiments. A large-scale numerical parametric study that is not constrained by experimental limitations such as container effects, motion orientation, and any impact of progressive shaking (Darby et al. 2019; Jones 2013) would be an important future work that will be carried out to further investigate and explore key features that control the reservoir's seismic response. The main findings from this study can be summarized as follows:

- The complex behavior of buried water reservoirs can be well-captured by high-fidelity numerical models that proved to be a valuable tool for performance-based design approaches.

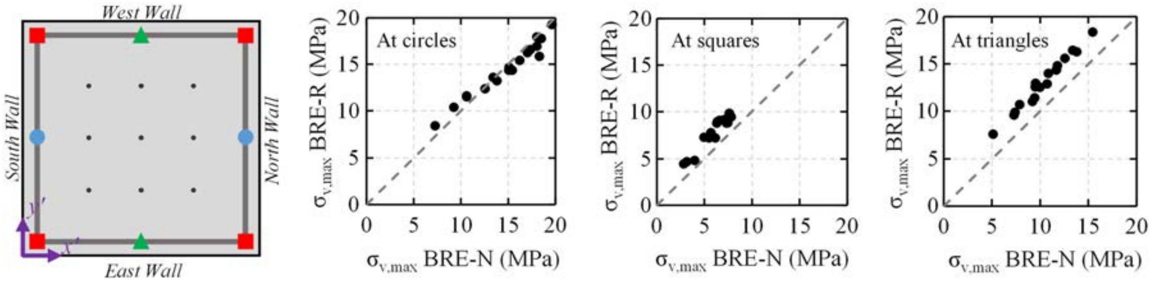

Fig. 17. Computed von Mises stress at the bottom of north and south walls, east and west walls, and corners.

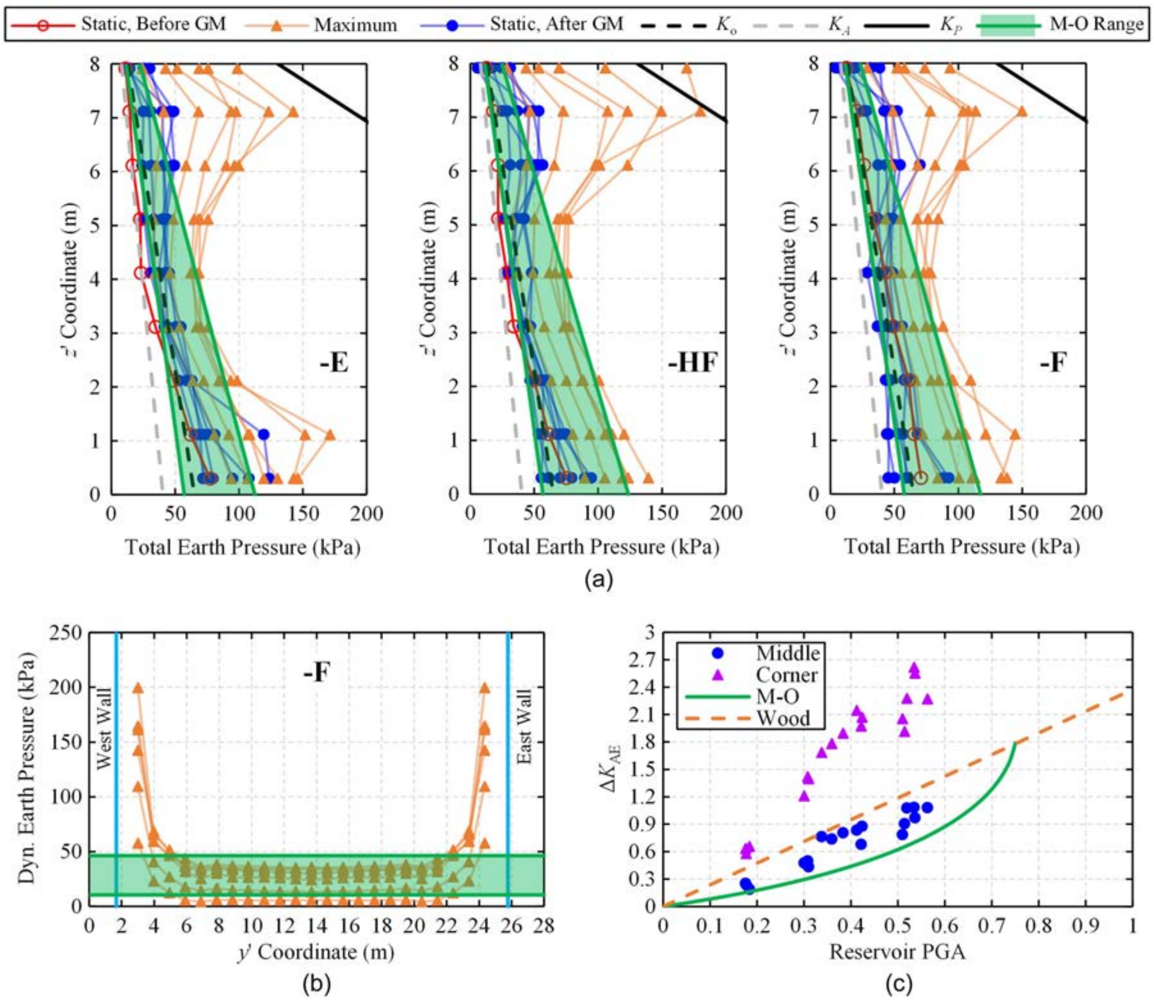

(a)

(b)

(c)

Fig. 18. Computed earth pressure at the north wall: (a) vertical distribution at $y' = 14$ m; (b) horizontal distribution at $z' = 4$ m; and (c) the ΔKAE as a function of reservoir PGA in comparison to M-O and Wood analytical solutions.

- The nature of the reservoir response is truly 3D. This is clearly observed by the nonuniform distribution of earth pressures, localized stress concentrations, water dynamic pressures, and the racking deformation shape of the roof.
- The roof slab acted as a diaphragm that distributed the lateral forces to the vertical structural elements based on their relative stiffnesses. It was found that the lateral forces were mainly resisted by the walls parallel to the motion direction and least resisted by the columns.
- When including a more realistic condition of 2D motion, a nonuniform stress distribution was observed, and demands were increased especially at the corners. Furthermore, the increase in water dynamic pressures was not symmetrical across the reservoir due to 2D motion effects.
- The case of the full reservoir was found to be the governing case in terms of base shear, induced bending moments, and racking deformation. The difference in the maximum base shear between the empty and the full reservoir cases was up to 25%.
- The case of the empty reservoir resulted in an increased base slippage due to the reduction in the interface frictional capacity. This may result in permanent differential movement and may adversely impact the reservoir functionality postearthquake.
- Earth pressures were found to fall between M-O and Wood solutions at the middle of the wall. However, higher earth pressures were computed near the corners of the reservoir due to arching effects.

The implications of the study findings on common design practice, along with some recommendations, are subsequently listed:

- It is common in practice to decouple the problem and evaluate demands separately (e.g., water pressure, earth pressure, etc.). Then, the demands would often be combined using the square root of square summation. It is clear now, based on what was previously presented, that the performance of the reservoir is complex and quite different than other underground structures. Decoupling the problem may under/overestimate the demands; thus, it is recommended to carry out an FSSI simulation to more reliably evaluate the demands.
- Simplified methods like M-O and Westergaard are extensively used in practice to evaluate the earth and water pressures, respectively. The designer may use simplified methods for preliminary design but should always consider doing an FSSI analysis to check the adequacy of the final design. Simplified methods do not consider the interaction between the different elements of the problem, do not give insights into the critical zones and the 3D response of the reservoirs, and ignore 2D motion effects.
- In literature, numerical models of the reservoir are often carried out using 2D slice models while assuming plane-strain conditions. The reservoir response was found to be 3D in nature.

It was shown that the reservoir roof acted as a diaphragm and the side walls were the main lateral resisting element. Carrying out a 2D slice model would ignore the walls' contribution and as such would overestimate the deformations and may underestimate the demands as the system becomes more flexible. Therefore, designers should always model the 3D geometry of the structure.

- Designers often opt to use 1D motion, especially when the structure is symmetrical. Applying 1D motion would underestimate the demands. When considering a 2D motion, demands were increased near the corners and, therefore, it's always recommended to include bidirectional shaking.
- Ignoring the presence of water in the design may underestimate the demands. The study showed that the presence of water increased the base shear, dynamic bending moment, and racking. Therefore, it is recommended to consider the effects of water and that is best done through FSSI simulations.
- Although the full case was shown to generate the highest demands, the empty case resulted in an increased base slippage, which may have certain structural and nonstructural implications to consider. Thus, it is a good practice to consider both cases—full and empty—in the seismic design.
- Racking stiffness and shape are shown to be nonuniform and, as such, differential movement should be accounted for in the design of structural and nonstructural elements.

Data Availability Statement

All experimental data are curated in DesignSafe and soon to be released along with an extensive report. Some or all numerical models or codes that support the findings of this study are available upon reasonable request to the corresponding author.

Acknowledgments

The authors gratefully acknowledge the funding provided by the National Science Foundation under Grants CMMI-1763129 and CMMI-1762749. The centrifuge facility at UC Davis is part of the NSF Natural Hazards Research Infrastructure (NHERI) program under Award CMMI-2037883. Any opinions, findings, conclusions, or recommendations expressed in this paper are solely those of the authors and do not necessarily reflect the views of the National Science Foundation. The authors thank the UC Davis Center for Geotechnical Modeling Associate Director Dr. Dan Wilson and staff (Tom Kohnke, Anatoliy Ganchenko, and Chad Justice) for making the experiments presented in this paper possible.

Supplemental Materials

Appendix S1, Tables S1–S5, and Figs. S1–S11 are available online in the ASCE Library (www.ascelibrary.org).

References

Al Atik, L., and N. Sitar. 2010. "Seismic earth pressures on cantilever retaining structures." *J. Geotech. Geoenviron. Eng.* 136 (10): 1324–1333. https://doi.org/10.1061/(ASCE)GT.1943-5606.0000351.

AlKhatib, K. 2023. "Seismic fluid-structure-soil interaction of buried water reservoirs." Ph.D. thesis, Dept. of Civil and Environmental Engineering, Univ. of Illinois Urbana-Champaign.

Bolton, M. 1986. "The strength and dilatancy of sands." *Géotechnique* 36 (1): 65–78. https://doi.org/10.1680/geot.1986.36.1.65.

Boulanger, R. W., M. Khosravi, A. Khosravi, and D. W. Wilson. 2018. "Remediation of liquefaction effects for an embankment using soil-cement walls: Centrifuge and numerical modeling." *Soil Dyn. Earthquake Eng.* 114 (Nov): 38–50. https://doi.org/10.1016/j.soildyn.2018.07.001.

Carey, T., A. Gavras, B. Kutter, S. Haigh, S. Madabhushi, M. Okamura, D. Kim, K. Ueda, W. Hung, and Y. Zhou. 2018. "A new shared miniature cone penetrometer for centrifuge testing." In *Proc., 9th Int. Conf. on Physical Modelling in Geotechnics (ICPMG 2018)*. London: CRC Press.

CH2MHILL. 2015. *Buried reservoir seismic program*. Seattle: CH2MHILL.

Cheng, P., P. Tehrani, M. McHenry, W. Bennett, D. Anderson, and R. Mitchell. 2017. "Performance based design with 3D dynamic SSI and FSI analyses for large buried water storage reservoirs." In *Proc., 3rd Int. Conf. on Performance-based Design in Earthquake Geotechnical Engineering (PBDIII)*. Vancouver, BC, Canada: International Society for Soil Mechanics and Geotechnical Engineering's Technical Committee TC203 on Earthquake Geotechnical Engineering (ISSMGE-TC203).

Chiang, D., and J. Beck. 1994. "A new class of distributed-element models for cyclic plasticity—I. Theory and application." *Int. J. Solid Struct.* 31 (4): 469–484. https://doi.org/10.1016/0020-7683(94)90087-6.

Darby, K. M., R. W. Boulanger, J. T. DeJong, and J. D. Bronner. 2019. "Progressive changes in liquefaction and cone penetration resistance across multiple shaking events in centrifuge tests." *J. Geotech. Geoenviron. Eng.* 145 (3): 04018112. https://doi.org/10.1061/(ASCE)GT.1943-5606.0001995.

Darendeli, M. B. 2001. "Development of a new family of normalized modulus reduction and material damping curves." Ph.D. thesis, Dept. of Civil, Architectural, and Environmental Engineering, Univ. of Texas at Austin.

Deng, Y., S. Dashti, A. Hushmand, C. Davis, and B. Hushmand. 2016. "Seismic response of underground reservoir structures in sand: Evaluation of Class-C and C1 numerical simulations using centrifuge experiments." *Soil Dyn. Earthquake Eng.* 85 (Apr): 202–216. https://doi.org/10.1016/j.soildyn.2016.04.003.

Garnier, J., C. Gaudin, S. M. Springman, P. Culligan, D. Goodings, D. Konig, B. Kutter, R. Phillips, M. Randolph, and L. Thorel. 2007. "Catalogue of scaling laws and similitude questions in geotechnical centrifuge modelling." *Int. J. Phys. Modell. Geotech.* 7 (3): 1–23. https://doi.org/10.1680/ijpmg.2007.070301.

Groholski, D. R., Y. M. Hashash, B. Kim, M. Musgrove, J. Harmon, and J. P. Stewart. 2016. "Simplified model for small-strain nonlinearity and strength in 1D seismic site response analysis." *J. Geotech. Geoenviron. Eng.* 142 (9): 04016042. https://doi.org/10.1061/(ASCE)GT.1943-5606.0001496.

Harounian, A., C. A. Davis, M. Lew, and M. B. Hudson. 2014. "Going beyond code-based design: Use of advanced numerical modeling to support design of Los Angeles's Headworks reservoir." In *Proc., Geo-Congress 2014*. Reston, VA: ASCE. https://doi.org/10.1061/9780784413272.296.

Hashash, Y. M., J. J. Hook, B. Schmidt, I. John, and C. Yao. 2001. "Seismic design and analysis of underground structures." *Tunnelling Underground Space Technol.* 16 (4): 247–293. https://doi.org/10.1016/S0886-7798(01)00051-7.

Hashash, Y. M. A., S. Dashti, M. Musgrove, K. Gillis, M. Walker, K. Ellison, and Y. I. Basarah. 2018. "Influence of tall buildings on the seismic response of shallow underground structures." *J. Geotech. Geoenviron. Eng.* 144 (12): 04018097. https://doi.org/10.1061/(ASCE)GT.1943-5606.0001963.

Hashash, Y. M. A., M. Musgrove, S. Dashti, and P. Cheng. 2017. "Seismic performance evaluation of underground structures—Past practice and future trends." In *Proc., 3rd Int. Conf. on Performance Based Design in Earthquake Geotechnical Engineering (PBD-III)*. Vancouver, BC, Canada: International Society for Soil Mechanics and Geotechnical Engineering's Technical Committee TC203 on Earthquake Geotechnical Engineering (ISSMGE-TC203).

Housner, G. W. 1957. "Dynamic pressures on accelerated fluid containers." *Bull. Seismol. Soc. Am.* 47 (1): 15–35. https://doi.org/10.1785/BSSA0470010015.

Hudson, M. B., C. A. Davis, M. Lew, and A. Harounian. 2014. "Seismic resilience design for a concrete box reservoir." In *Proc., 6th China-Japan-US Trilateral Symp. on Lifeline Earthquake Engineering*. Beijing: Beijing Univ. of Technology. https://doi.org/10.1061/9780784413234.018.

Hushmand, A., S. Dashti, C. Davis, B. Hushmand, M. Zhang, M. Ghayoomi, J. McCartney, Y. Lee, and J. Hu. 2016. "Seismic performance of underground reservoir structures: Insight from centrifuge modeling on the influence of structure stiffness." *J. Geotech. Geoenviron. Eng.* 142 (7): 04016020. https://doi.org/10.1061/(ASCE)GT.1943-5606.0001477.

Iwan, W. D. 1967. "On a class of models for the yielding behavior of continuous and composite systems." *J. Appl. Mech.* 34 (3): 612–617. https://doi.org/10.1115/1.3607751.

Jennings, P. C. 1971. *Engineering features of the San Fernando earthquake of February 9, 1971 report*. Pasadena, CA: California Institute of Technology.

Jones, K. C. 2013. "Dynamic soil-structure-interaction analysis of structures in dense urban environments." Ph.D. thesis, Dept. of Civil and Environmental Engineering, Univ. of California.

Kenmir, R. C. 1968. "Concrete reservoir design." *J. Am. Water Works Assoc.* 60 (10): 1181–1194. https://doi.org/10.1002/j.1551-8833.1968.tb03660.x.

LSTC (Livermore Software Technology Corporation). 2020. *LS-Dyna keyword user's manual*. Chicago: LSTC.

Menq, F.-Y. 2003. "Dynamic properties of sandy and gravelly soils." Ph.D. thesis, Dept. of Civil, Architectural, and Environmental Engineering, Univ. of Texas at Austin.

Montoya, B. M., R. Gerhard, J. T. DeJong, D. W. Wilson, M. H. Weil, B. C. Martinez, and L. Pederson. 2012. "Fabrication, operation, and health monitoring of bender elements for aggressive environments." *Geotech. Test. J.* 35 (5): 728–742. https://doi.org/10.1520/gtj103300.

Morales, B. 2020. "Centrifuge modeling of hydrodynamic loads in water storage tanks." M.S. thesis, Dept. of Civil and Environmental Engineering, Univ. of California.

Ng, C. W. W. 2014. "The state-of-the-art centrifuge modelling of geotechnical problems at HKUST." *J. Zhejiang Univ. Sci. A* 15 (1): 1–21. https://doi.org/10.1631/jzus.A1300217.

Numanoglu, O. A., Y. M. Hashash, S. M. Olson, A. Cerna-Diaz, C. J. Rutherford, L. Bhaumik, and T. Weaver. 2023. "A simplified three-dimensional constitutive model for seismic modeling of dense sands." *Soil Dyn. Earthquake Eng.* 167 (Aug): 107794. https://doi.org/10.1016/j.soildyn.2023.107794.

Numanoglu, O. A., M. Musgrove, J. A. Harmon, and Y. M. Hashash. 2017. "Generalized non-Masing hysteresis model for cyclic loading." *J. Geotech. Geoenviron. Eng.* 144 (1): 06017015. https://doi.org/10.1061/(ASCE)GT.1943-5606.0001816.

Okabe, S. 1924. "General theory on earth pressure and seismic stability of retaining wall and dam." *J. Jpn. Soc. Civ. Eng.* 10 (6): 1277–1323.

Phillips, C., and Y. M. Hashash. 2009. "Damping formulation for nonlinear 1D site response analyses." *Soil Dyn. Earthquake Eng.* 29 (7): 1143–1158. https://doi.org/10.1016/j.soildyn.2009.01.004.

Seed, H. B., and R. V. Whitman. 1970. "Design of earth retaining structures for dynamic loads." In *Proc., ASCE Specialty Conf.-Lateral Stress in the Ground and Design of Earth Retaining Structures*. Reston, VA: ASCE.

Sinha, S., K. Ziotopoulou, and B. Kutter. 2021. *Centrifuge testing of liquefaction-induced downdrag on axially loaded piles: Data report for SKS02*. Rep. No. UCD/CGMDR–21/01. Davis, CA: Univ. of California.

Taylor, R. N. 2018. *Geotechnical centrifuge technology*. London: CRC Press. https://doi.org/10.1201/9781482269321.

Wang, J.-N. 1993. *Seismic design of tunnels: A simple state-of-the-art design approach*. New York: Parsons Brinckerhoff.

Wilson, D. W., R. W. Boulanger, B. L. Kutter, and A. Abghari. 1997. "Aspects of dynamic centrifuge testing of soil-pile-superstructure interaction." In *Observation and modeling in numerical analysis and model tests in dynamic soil-structure interaction problems*. Reston, VA: ASCE.

Wood, J. H. 1973. "Earthquake induced soil pressures on structures." Ph.D. thesis, Earthquake Engineering Research Laboratory, California Institute of Technology.

Zhang, W., E. E. Seylabi, and E. Taciroglu. 2017. "Effects of soil stratigraphy on dynamic soil-structure interaction behavior of large underground structures." In *Proc., 3rd Int. Conf. on Performance-based Design in Earthquake Geotechnical Engineering (PBDIII)*. Vancouver, BC, Canada: International Society for Soil Mechanics and Geotechnical Engineering's Technical Committee TC203 on Earthquake Geotechnical Engineering (ISSMGE-TC203).